Explaining Bayesian Neural Networks

Anonymous authors
Paper under double-blind review

Abstract

To advance the transparency of learning machines such as Deep Neural Networks (DNNs), the field of explainable AI (XAI) was established to provide interpretations of DNNs' predictions. While different explanation techniques exist, a popular approach is given in the form of attribution maps, which illustrate, given a particular data point, the relevant patterns the model has used for making its prediction. Although Bayesian models such as Bayesian Neural Networks (BNNs) have a limited form of transparency built-in through their prior weight distribution, they lack explanations of their predictions for given instances. In this work, we bring together these two perspectives of transparency into a holistic explanation framework for explaining BNNs.Within the Bayesian framework, network weights follow a probability distribution; hence the standard point explanation extends to an *explanation distribution*. Viewing explanations probabilistically, we *aggregate* and *analyze* multiple local attributions drawn from an approximate posterior to surface *explanation diversity*. This diversity provides a diagnostic lens on how predictive rationales can vary across posterior samples. Quantitative and qualitative experiments on toy/benchmark data and real-world pathology illustrate that our framework enriches standard explanations with uncertainty information and supports practical inspection of explanation stability.

1 Introduction

Deep Neural Networks (DNNs) have achieved significant success over the years, helping to advance Artificial Intelligence (AI). Driven by the exponential growth in available data and computational resources, DNNs achieve state-of-the-art results across various fields of Machine Learning (ML), surpassing human performance in various domains tasks (Silver et al., 2016; Merchant et al., 2023; He et al., 2015; Vinyals et al., 2017; Liu et al., 2019; Won et al., 2020) and, recently, demonstrating emerging general reasoning abilities with the advances of Large Language Models (LLMs) (Bubeck et al., 2023). DNNs accomplish such high performance by learning mappings from raw data to meaningful representations.

With the increasing complexity of modern Neural Networks, it is a difficult task to explain their decision-making process. Therefore, DNNs have often been considered as "black-box" (Vidovic et al., 2015; Buhrmester et al., 2019). However, especially in security-critical applications (such as autonomous driving or medicine), transparency of the decision-making model is mandatory and therefore the network's inability to explain its predictions restricts the applicability of ML systems. Indeed, despite showing great performance in test environments, DNNs have not yet reached universal acceptance in the above-mentioned areas (Buch et al., 2018). Furthermore, recent studies have confirmed that frequently DNNs are susceptible to learning *spurious correlations* (Geirhos et al., 2020). These correlations, often arising from chance occurrences or the presence of specific artifacts, are not intended and have undesirable consequences, resulting in poor generalization and potential risks. This phenomenon, termed the *Clever Hans* effect (Lapuschkin et al., 2019) holds significant importance due to its widespread prevalence among various models and datasets (Izmailov et al., 2022). Notably, a substantial number of models trained on the ImageNet dataset (Deng et al., 2009) display reliance on watermarks in Chinese language watermarks (Bykov et al., 2023d), significantly impairing their performance (Li et al., 2023).

The field of *Explainable AI (XAI)* has emerged to address these concerns (see e.g. Samek et al. (2019)). XAI aims to develop and study methodologies for explaining the predictions made by advanced learning

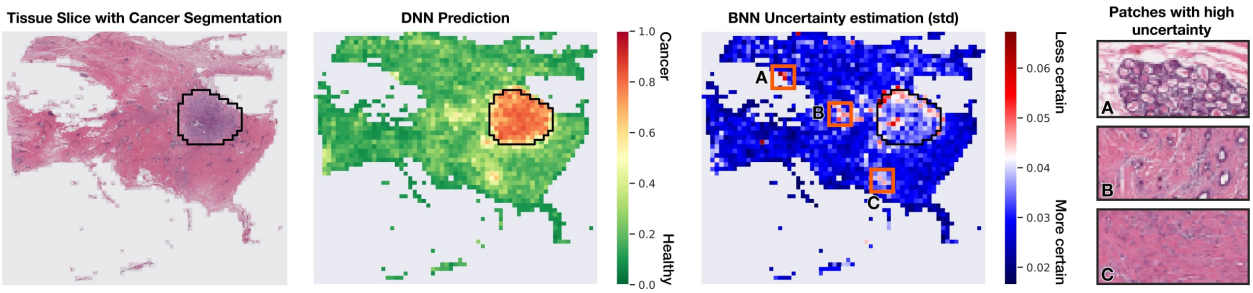

Figure 1: Illustrating the practical advantages of BNNs over standard DNNs. From left to right: a whole-slide image from a cancer patient, divided into patches with highlighted cancerous regions; DNN prediction; BNN uncertainty estimation; and patches with the highest uncertainty. Unlike a standard DNN, the BNN provides uncertainty estimates for each patch. Blue indicates high certainty, while red indicates low certainty. The rightmost panel shows patches where the model's prediction is uncertain and fluctuates between classes.

machines such as DNNs. Recent advances in XAI have led to a variety of novel methods (Saleem et al., 2022; Adadi & Berrada, 2018; Das & Rad, 2020; Tjoa & Guan, 2020). These can be grouped into *global* and *local* explanation methods. While global explanation methods interpret the decision-making of DNNs across a population by visualizing the signals that cause significant activation in a neuron (Erhan et al., 2009; Nguyen et al., 2016), analyzing relationships between neurons (Bykov et al., 2023a;b) or by linking the neuron's learned concepts to human-understandable concepts (Bykov et al., 2023c; Bau et al., 2017; Mu & Andreas, 2020; Oikarinen & Weng, 2022), local explanations provide interpretations of the prediction for a particular data example by attributing relevances to the input features (Baehrens et al., 2010; Bach et al., 2015; Selvaraju et al., 2017; Yosinski et al., 2015; Kindermans et al., 2017; Montavon et al., 2018; Lundberg & Lee, 2017; Lundberg et al., 2020; Dombrowski et al., 2021).

Most of the explanation methods, local and global ones, are developed for DNNs trained in a *maximum-a-posteriori* (MAP) setting, where the weights of the model are point estimates. In contrast, Bayesian Neural Networks (BNNs) learn a distribution of the network weights, which induces also a distribution on the prediction. For a better intuition on the advantage in explainability of a BNN over a DNN, we consider the example image shown in Figure 1, where a histopathological image (Janowczyk & Madabhushi, 2016; Cruz-Roa et al., 2014) taken from a cancer patient (see e.g. (Klauschen et al., 2018; Hägele et al., 2020; Binder et al., 2021)) is shown on the left. Starting from this whole slide image, smaller patches are extracted and fed into a DNN, trained to classify patches into cancer or non-cancer. In the center of Figure 1, we show the prediction score of a regular (non-Bayesian) DNN for the class *cancer*. While these scores are usually normalized with a softmax function, these scores do not represent actual probabilities (Hendrycks & Gimpel, 2016) — the DNN provides no further information on how certain or uncertain the patches' relevances are for the prediction. This additional information is provided by BNNs, e.g. in the form of the variances shown on the right in Figure 1. We observe that there are distinct regions where the model is significantly more certain about a patch indicating cancerous areas (highlighted in blue colors) than in other regions (highlighted in red, referring to the most uncertain regions).

Thus, BNNs provide predictive uncertainty, but—like standard DNNs—do not yield local explanations out of the box. Our contribution is a practical, method-agnostic framework that translates predictive *epistemic* uncertainty into *explanation* uncertainty: a distribution over attribution maps that can be summarized by mean and percentile-based aggregations and analyzed via clustering. The goal is to *visualize and quantify* variability in explanatory rationales under an approximate posterior, not to claim identification of ground-truth decision modes. Importantly, the computational overhead of our aggregation scales *linearly* with the number of posterior samples N (i.e., N base attributions plus a constant-time aggregation), and for lightweight approximations such as MC Dropout the per-sample inference cost differs marginally from deterministic models. Our model is even applicable to regular DNNs (e.g., CNNs) trained in a non-Bayesian fashion, which can first be translated into BNNs (e.g., using MC dropout (Srivastava et al., 2014) or Laplace approximation (De Laplace, 1774; Ritter et al., 2018)), and then using our proposed method for a rigorous

explanation. Thus our approach can enrich the explanation of regular DNNs with additional uncertainty information.

To illustrate this advantage, consider again the medical task illustrated in Fig 1. The first step towards transparency of the shown model is assigning the input features with relevance scores; this is what explanation methods of regular DNNs do. It helps to identify the areas in the image that were relevant for the prediction. Our BNN explanation would additionally provide information on regions where the method is confident about the relevance scores. This may enable an expert to faster identify the most significant cancer areas in an image. On the other hand, the expert might want to look specifically into areas of low confidence to resolve this low confidence by contributing with human expert knowledge to cancer image evaluation. Hence, by determining the level of certainty required by a particular case or by visualizing multiple levels of certainty at once in an explanation, our method can lead to additional insight into the underlying prediction strategy of a model.

In this work, we will propose and investigate different techniques for explaining the decision-making process of (deep) BNNs. Our approach is method-agnostic, i.e. it can build on any arbitrary explanation method for regular (non-Bayesian) *DNNs*, which are transformed into a local attribution method for *BNNs*. The proposed method can be combined with any (approximate) inference procedure of BNNs. In computational experiments, our approach interestingly revealed that BNNs implicitly employ multiple heterogeneous prediction strategies. The reason is that BNNs exhibit numerous modes, and approximately one can think of a mode as a prototypical prediction strategy. In contrast, in a standard non-Bayesian DNN, the prediction is deterministic and thus cannot extract multi-modal explanations. With our proposed method, we are now able to visualize the different modes thus revealing the intrinsic multi-modality in the decision-making of BNNs (and by association: DNNs).

In the following, we summarize the main contributions of this work:

- **Mean explanation under an approximate posterior:** we give conditions under which the explanation of the predictive mean equals the mean of explanations (Lemma 4.1, Theorem 4.1).
- **UAI (Union/Intersection) aggregations:** percentile-based summaries that expose stable vs. opportunistic features and yield uncertainty-aware heatmaps (including UAI$^+$).
- **Explanation diversity as a diagnostic:** clustering sampled explanations to *surface* diverse explanatory patterns under the chosen posterior approximation.
- **Generality & cost:** the framework is method- and inference-agnostic and adds only *linear* overhead $O(N \cdot C_{\text{attr}})$ (with C_{attr} the cost of the base attribution).

2 Background and Related Work

This section provides a comprehensive overview of BNNs and well-established local explanation methods.

2.1 Bayesian Neural Networks

From a statistical perspective, standard DNNs are usually trained using *maximum a-posteriori (MAP) optimization* (Wilson, 2020):

$$\begin{aligned} \hat{W} &= \text{argmax}_W \log p(W \mid \mathcal{D}_{\text{tr}}), \\ &= \text{argmax}_W \log p(\mathcal{D}_{\text{tr}} \mid W) + \log p(W), \end{aligned} \tag{1}$$

which reduces to the maximum likelihood estimation when the prior distribution $p(W)$ is flat. The most commonly used loss functions and regularizers fit into this framework, such as categorical cross-entropy for classification or mean squared error for regression. Although this procedure is efficient since the networks only learn a fixed set of weights, it does not provide uncertainty information about the learned weights and subsequently on the prediction. In contrast, Bayesian neural networks (BNNs) estimate the posterior

distribution of weights, and thus, provide uncertainty information on the prediction, which can provide confidence information on predictions. Particularly, in critical real-world applications of deep learning—for instance, medicine (Hägele et al., 2020; Holzinger et al., 2019; Klauschen et al., 2018) and autonomous driving (Koo et al., 2015; Wiegand et al., 2019)—where predictions need to be highly precise and wrong predictions could easily be fatal, the availability of prediction uncertainties can be of fundamental advantage.

Let $f_W : \mathbb{R}^d \to \mathbb{R}^k$ be a feed-forward neural network with the weight parameter $W \in \mathcal{W}$. Given a training dataset $\mathcal{D}_{\text{tr}} = \{x_n, y_n\}_{n=1}^N$, Bayesian learning (approximately) learns the posterior distribution

$$p\left(W|\mathcal{D}_{\text{tr}}\right) = \frac{p(\mathcal{D}_{\text{tr}}|W)p(W)}{\int_{\mathcal{W}} p(\mathcal{D}_{\text{tr}}|W)p(W)dW} \ , \tag{2}$$

where $p(W)$ is the prior distribution of the weight parameter. After training, the output for a given test sample x is predicted by the distribution:

$$p(y|x, \mathcal{D}_{\text{tr}}) = \int_{\mathcal{W}} p(y|f_W(x))p(W|\mathcal{D}_{\text{tr}})dW. \tag{3}$$

Since the denominator of the posterior, shown in equation 2, is intractable for neural networks, numerous approximation methods have been proposed, e.g., Laplace approximation (Ritter et al., 2018), Variational Inference (Graves, 2011; Osawa et al., 2019), MC dropout (Gal & Ghahramani, 2016), Variational Dropout (Kingma et al., 2015; Molchanov et al., 2017), MCMC sampling (Wenzel et al., 2020), and SWAG (Maddox et al., 2019; Wilson & Izmailov, 2020). With these approximation methods, one can now efficiently draw samples from the approximate posterior distribution of the network parameters (equation 3), and compute statistics, e.g., mean and variance, of the prediction for a given data point x. Classical MAP training procedures could also be seen as performing approximate Bayesian inference, using the approximate posterior $p(W|\mathcal{D}_{\text{tr}}) \approx \delta(W = \hat{W})$, where δ is the Dirac delta function.

2.2 Local attribution methods

Local explanation methods attribute *relevance* to the input (features) or intermediate nodes (Bach et al., 2015; Vidovic et al., 2016; Selvaraju et al., 2017; Montavon et al., 2018) by using a relevance attribution operation, which we define as follows:

Definition 2.1 (Relevance Attribution operator)**.** An operator $\mathcal{T}_{x,W}[\cdot]$ that maps an output function $f_W : \mathbb{R}^d \to \mathbb{R}^k$ to a relevance function $R : \mathbb{R}^d \to \mathbb{R}^d$ is called a relevance attribution operator:

$$R_W(x) = \mathcal{T}_{x,W}[f_W](x). \tag{4}$$

The above definition postulates that the relevance of an input feature/node depends on the input mainly via the output function, although it can have a direct dependence on x and W.

In this paper, we demonstrate our novel BNN explanation framework mainly using Layer-wise Relevance Propagation (LRP) (Bach et al., 2015) as the base explanation method, however, we would like to stress that our BNN explanation framework can be applied for *any* existing explanation method.

Gradient explanation The Gradient explanation method, i.e. $\mathcal{T}_{x,W} = \nabla_x$, where ∇_x is the weak derivative w.r.t. x, is one of the most basic explanation methods. It visualizes the possible extent of change made by the predictive function in a local neighborhood around the original datapoint $\boldsymbol{x}$ (Erhan et al., 2009; Baehrens et al., 2010; Simonyan et al., 2013).

LRP Layer-wise Relevance Propagation (Bach et al., 2015) is a model-aware explanation technique that can be applied for feed-forward neural networks and can be used for different types of inputs, such as images, videos, or text (Anders et al., 2019; Arras et al., 2017; Montavon et al., 2018; Binder et al., 2021). The underlying idea of the LRP algorithm is to use the network weights and the neural activations computed in the forward-pass to propagate the relevant output back through the network until the input layer is reached. This propagation procedure is subject to a conservation rule — analogous to Kirchoff's conservation laws in

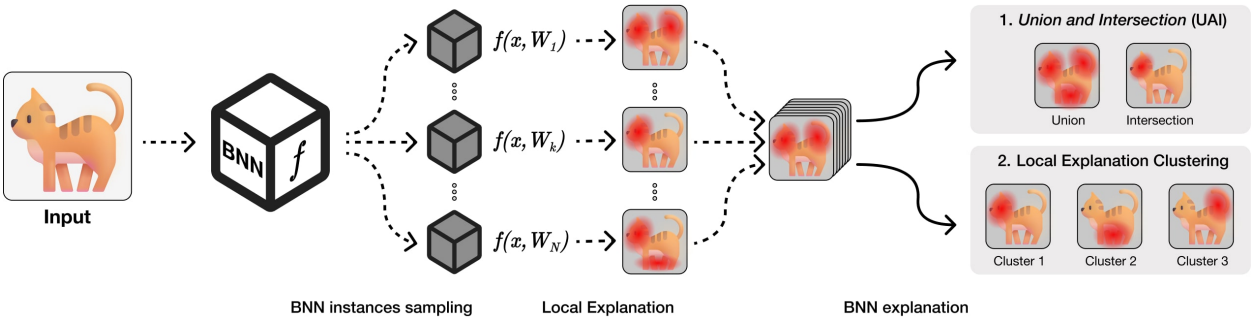

Figure 2: Schematic illustration of proposed methods for explaining Bayesian Neural Networks. Given a particular input – a cat image – we sample models from the posterior distribution and collect local explanations from each instance. These explanations are later aggregated using *Union and Intersection* (UAI) method: The Union explanation provides a global overview of the features learned by the BNN by combining various modes, whereas the intersection explanation provides the intersection strategy used by the BNN – demonstrating the most certain features used for the prediction. Further, local explanations can be clustered to illustrate the different modalities of the decision-making strategies.

electrical circuits (Montavon et al., 2019) — in each backpropagation step, the relevances from the output layer are distributed towards the input layer, while the sum of relevances should remain the same. Existing variations of LRP are, e.g., LRP-0, LRP-ε, LRP-γ, and LRP-CMP (Bach et al., 2015; Montavon et al., 2019).

Integrated gradients Integrated Gradients (Sundararajan et al., 2017) is an axiomatic local explanation algorithm that also addresses the "gradient saturation" issue (Samek et al., 2016). It assigns relevance scores to each feature by approximating the integral of the gradients of the model output with respect to a scaled version of the input. The relevance attribution function, in this case, can be defined as

$$\mathcal{T}_{x,W}[f_W](x) = (x - \bar{x}) \odot \int_0^1 \frac{\partial f_W(\bar{x} + \alpha(x - \bar{x}))}{\partial x} d\alpha,$$

where $\odot$ denotes the element-wise product, and $\bar{x}$ is a *reference point* that represents the absence of a feature in the input.

3 XAI for BNNs

Despite the growing interest in Explainable AI, *Bayesian Neural Networks (BNN)* have so far lacked the attention of the XAI community. Most of the work on the topic of interpreting the BNNs concentrate on uncertainty quantification and visualization: (Kwon et al., 2020) proposes a method to decompose the moment-based predictive uncertainty into two parts: aleatoric and epistemic: in (Chai, 2018) author proposes a model-agnostic method to visualize the contribution of individual features to predictive, epistemic and aleatoric uncertainty (Kwon et al., 2020). Recently, it has been shown that explanations of DNN can be enhanced by introducing stochasticities to the model weights (Bykov et al., 2021), which, to some extent, lead to explanations similar to the ones using Diagonal or KFAC Laplace approximation. The so-called NoiseGrad method (Bykov et al., 2021) adds multiplicative Gaussian noise to the model weights, which significantly reduces the gradient shattering effect (Samek et al., 2021b) similar to the SmoothGrad method (Smilkov et al., 2017). However, beyond uncertainty, BNNs offer a principled way to capture model variability, making them a valuable target for explainability research (Grinwald et al., 2023). Understanding not only what the model predicts, but also how confident and stable those predictions are across weight distributions, is essential for trustworthy AI.

4 Explaining Bayesian Neural Networks

In the following, we consider a neural network $f_W(x)$ and a relevance function $R_W(x)$ (defined in equation 10), using an arbitrary explanation method. Note that $R_W(x)$ is a deterministic mapping for a fixed parameter W. Therefore, the posterior distribution of parameter W induces a distribution over the relevances, resulting in a distribution over relevance maps. Given the posterior distribution of $W \sim p(W|\mathcal{D}_{\text{tr}})$, we can define the distribution of relevance as

$$p(R|\boldsymbol{x}, \mathcal{D}_{\text{tr}}) = \int R_W(x) p(W|\mathcal{D}_{\text{tr}}) dW. \tag{5}$$

The relevance samples

$$R \sim p(R|\boldsymbol{x}, \mathcal{D}_{\text{tr}})$$

can be obtained by drawing weights from the posterior distribution:

$$W \sim p(W|\mathcal{D}_{\text{tr}}).$$

A schematic illustration of the process of obtaining the explanations, as well as a high-level overview of proposed methods, is given in Figure 2. Here, illustratively, we can observe that different samples of the network lead to different explanations of the same input image. By applying aggregation strategies, such as the Intersection, Average, and Union strategies, the model behavior can be mapped more profoundly and can thus serve as support for an improved human understanding of the model's prediction strategy.

4.1 Average Explanation

For some conditions, the average relevance attribution coincides with the relevance attribution of the average prediction, which we state in the following Lemma:

Lemma 4.1. *For any explanation method that can be formalized as in equation 10 with a linear operator $\mathcal{T}_{x,W} = \mathcal{T}_x$ that does not depend on W, it holds that*

$$\mathcal{T}_x \left[\mathbb{E}_W \left[f_W\right]\right](x) = \mathbb{E}_W \left[\mathcal{T}_x[f_W](x)\right] = \mathbb{E}_W \left[R_W(x)\right]. \tag{6}$$

The claim is held trivially by the linearity assumption. Equation 6 in the above Lemma holds for some existing explanation methods, including LRP-0, which is known to be expressed as equation 10 with $\mathcal{T}_{x,W}[f_W](x) = \mathcal{T}_x[f_W](x) = x \odot \nabla_x[f_W](x)$. One can still rely on equation 10 under a slight violation of linearity.

Theorem 4.1. *Equation 6 holds almost everywhere in $x \in \mathbb{R}^d$ for LRP-0 with ReLU networks, gradient explanation, and IG.*

The proof is given in the Appendix. Theorem 4.1 states that the explanation of the predictive mean (LHS of equation 6) can be computed by the sample mean of the relevance maps over the posterior distribution (RHS of equation 6).

This is beneficial since it is computationally exhausting to explain the approximate mean predictive function directly (this requires simultaneously storing all the parameters along with their computational graphs for each of the samples from the posterior distribution), using the results from Theorem 4.1 we can now easily explain it by sampling relevance maps, which drastically eases the process.

4.2 Exploring multi-modality of explanations

As a result of the non-linear network activations, BNNs are known to have multi-modal predictive functions (Bishop, 2006). Different parameters sampled from an *approximate* posterior can yield noticeably different local attributions for a fixed input (Fig. 2). Consequently, naive averaging can obscure meaningful variability. We therefore cluster sampled explanations to *summarize* explanatory patterns under the chosen approximation. We do not assume that clusters correspond to distinct posterior *modes*; rather, they provide a diagnostic lens on explanation diversity.

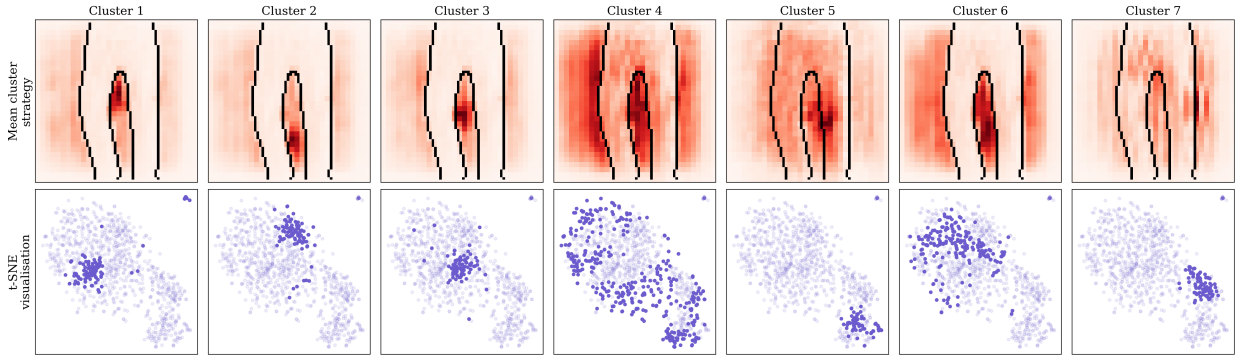

Figure 3: Visualization of the multi-modality of gradient explanations of a BNN (here a LeNet network trained with dropout) is shown exemplarily for an image of class "Trousers" from the Fashion MNIST dataset. The explanations were clustered by the SpRAy algorithm into 7 clusters, stated on top, and the first row shows the mean explanation for each cluster respectively, where the shape of the trousers is overlaid over the explanation. The second row depicts the t-SNE visualization of the distribution of explanations, where the points of the particular clusters are highlighted. From the mean cluster explanations, we can observe the variability in the decision-making process of the Bayesian Neural Networks — each mode illustrates one decision-making pattern and the number of elements in each cluster indicates the importance of each cluster to the prediction.

To investigate the "prime" strategies of the Bayesian learning machine and to decompose the behavior of BNNs into groups of inter-similar strategies, we propose to cluster the sampled explanations. Although our method does not restrict a user in choosing an algorithm for clustering, we propose to use the SpRAy (Spectral Relevance Analysis) clustering method. This method was initially introduced in (Lapuschkin et al., 2019) to solve a similar task — an analysis of the class-wise learned decision strategies of DNN in order to obtain a global view on the class related relevant patterns, which also supports the identification of undesirable behavior, such as Clever Hans artifacts (see Section 6.4 for more information about Clever Hans behavior). Note that SpRAy originally was constructed to investigate the typical traits in the decision-making process over a large collection of relevance maps, that were obtained from different data points from the training dataset. In contrast to the original setting of SpRAy, we exhibit and identify typical as well as atypical behavior in the BNN decision-making process for a *single* input image.

Once the clustering has been performed, "prime" prediction strategies of the BNN for the given input image can be identified by the cluster-wise average explanations. Moreover, the number of saliency maps in each cluster (normalized by the number of sampled relevance maps) could be considered as the "strength" of each strategy. We could visualize the explanations, clusters, and average cluster strategies in a two-dimensional embedding using a t-SNE plot (Maaten & Hinton, 2008) as shown in Figure 3, where the explanations of the Fashion MNIST (Xiao et al., 2017) input image is mainly divided into seven different clusters, which indicates the patterns of the main modes of the BNN. More practical details about the clustering process can be found in the appendix.

4.3 Union and Intersection Explanation

Grasping the multimodality of the network through explanations can be done in several ways. Each relevance attribution map is an explanation for an individual instance of the Bayesian Neural Network. In our work, we observed that differences between instances of BNN are reflected in the multi-modal distribution of explanations. Therefore, to aggregate differences in explanations for Bayesian Neural Networks, we propose a method called **UAI**: Union and Intersection. The intuitive idea is illustrated in Figure 2. We treat the relevance of a BNN as a random variable that follows equation 5.

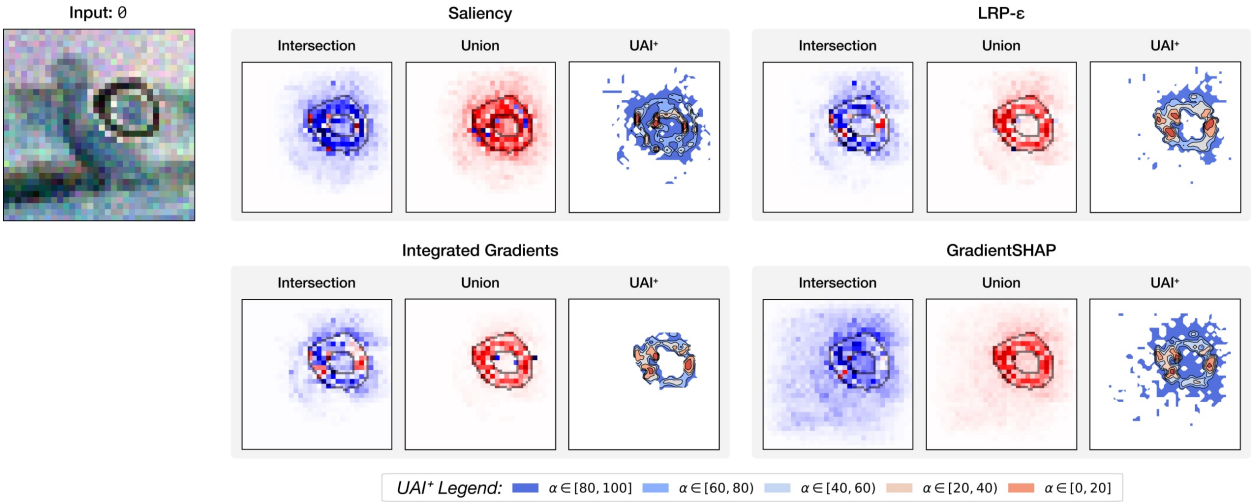

Figure 4: Illustrative explanations of a Bayesian Neural Network. The BNN was trained with Dropout on the Custom MNIST dataset (Bykov et al., 2021). The input, an MNIST digit zero on a random CIFAR Background is shown on the left and was correctly classified as zero by the BNN. Explanations of the BNN decision are given as Intersection ($\alpha = 5$), Average, Union ($\alpha = 95$), and UAI$^+$ explanations using LRP-ε (first row), Integrated Gradient (IG) (second row). We can observe that the relevance of all explanations correctly emphasizes the digit. However, our proposed Union and Intersection approach, in which the bundled information is contained in the UAI$^+$ explanation, has a stronger informational content about the role of the features concerning the model prediction by specifying the models (un)certainty that a feature contributed to the prediction made.

Given this distribution of relevance maps $p(R|\boldsymbol{x}, \mathcal{D}_{\text{tr}})$, we capture the uncertainty information of the BNN as follows:

$$\text{UAI}_\alpha(x) = \mathcal{P}_\alpha \left[p(R|\boldsymbol{x}, \mathcal{D}_{\text{tr}}) \right], \tag{7}$$

where $\mathcal{P}_\alpha$ is an operator computing the entry-wise (e.g. pixel-wise in the case of images) percentiles.

High percentiles ($\alpha > 0.5$) correspond to what we introduce as Union explanation – a resulting relevance map consisting of an accumulation of features of various relevance maps, i.e., providing information across modes of the BNN by allocating relevance to features that were considered of high importance by at least a small proportion of samples. In contrast to the Union explanation, small percentiles ($\alpha < 0.5$) illustrate the intersection of features, where at least 95% of explanations agree. For visualisations, we define Union explanations with $\alpha = 0.95$ and Intersection explanations with $\alpha = 0.05$

Furthermore, we introduce UAI^+_α, as the uncertainty information of the BNN relating to positive class attributions only:

$$\text{UAI}^+(x) = \mathcal{F}_\epsilon \left[p(R|\boldsymbol{x}, \mathcal{D}_{\text{tr}}) \right], \tag{8}$$

where $\mathcal{F}_\epsilon$ is an operator computing the entry-wise (pixel-wise) probabilities of relevance attributed to a particular pixel being less than some small predefined value $\epsilon > 0$. All proposed approaches (Intersection, Average, Union, and UAI$^+$) are method-agnostic, and the resulting LRP-ϵ and IG explanations are illustrated in Figure 4 for the case of an MC Dropout network.

As scales of various explanation methods differ, instead of thresholding significant positive relevances by fixing ϵ, we perform a *group normalization*: we normalize all positive relevances in all sampled attributions R_i by the maximum relevance value:

$$R_i^* = \frac{R_i}{\max\left(r_i^j | r_i^j \in R_i \ \forall i \in [1, N] \ \forall j \in [1, d] \right)}, \tag{9}$$

where N is the number of sampled attributions from the posterior and d is the number of features of the input. This way, we can set ϵ to a small value on the scale of [0,1], such that it will threshold only significant positive relevances. In our visualisations, we set $\epsilon = 0.05$ as we empirically observe this value to be the borderline of visual recognition of positive relevances in the attribution map.

4.4 Computational complexity

Let C_{attr} denote the cost of one base attribution on a deterministic network. Our framework draws N posterior samples and computes N attributions, then applies constant-time, entry-wise aggregations (percentiles or averages). Thus, the total cost is

$$\underbrace{O(N \cdot C_{\text{attr}})}_{\text{attributions}} + \underbrace{O(d\, N \log N)}_{\text{percentiles (optional)}} ,$$

where d is the number of input features (e.g., pixels). For MC Dropout, each forward pass adds only Bernoulli mask sampling and element-wise masking, so C_{attr} is close to the deterministic cost. The choice of posterior approximation is orthogonal to our method; more expensive samplers (e.g., HMC) increase C_{attr} proportionally.

5 Evaluation procedure

In the following, we provide the methodology of the qualitative and quantitative evaluation.

5.1 Qualitative Evaluation

For visual inspection of the results, we normalize the relevance maps with the MinMax transformation (Bach et al., 2015), which maps positive relevances onto the interval $[0, 1]$ and negative ones to $[-1, 0]$. Afterwards, the normalized relevance maps are visualized using the *'seismic'* colormap[1], which attributes red tones to pixels with positive relevances and blue tones to pixels with negative relevances.

5.2 Quantitative evaluation

For quantitative evaluation we use the localisation criterion, where we are interested in measuring the ability of an explanation method to attribute positive relevance to the object of interest. Hence, exemplary, if the prediction of a model is "cat", we assume that in the given image parts of the object cat are responsible for the prediction and subsequently yield positive relevance attribution by the explanation method. Thus, in order to correctly measure the ability of the method to "find" the object of interest, ground-truth segmentations are required (Arras et al., 2020; Lapuschkin et al., 2016; Kohlbrenner et al., 2020; Zhang et al., 2018; Fawcett, 2006; Bykov et al., 2021).

To measure the localization capability of an explanation method, we employ two different metrics, Area Under the ROC Curve and Relevance Mass Accuracy (Arras et al., 2020).

- **AUC ROC**: For each explanation (e.g., in form of a heatmap), we calculate the area under the receiver operating characteristic in order to measure how closely the areas of greatest relevance of the explanation correspond to the classified object. Note that for computing the AUC value, the pixel-wise ground-truth segmentation of the object serve as the true label information, whereas the relevance information from the explanation serve as the predicted label information.
- **Relevance Mass Accuracy (MA)**: For each explanation, we measure the proportion of the relevance mass that lies on the object in comparison to the total relevance mass:

$$MA = \frac{\sum_{i \in O} R_i}{\sum_{j \in I} R_j},$$

[1] https://matplotlib.org/3.1.0/tutorials/colors/colormaps.html

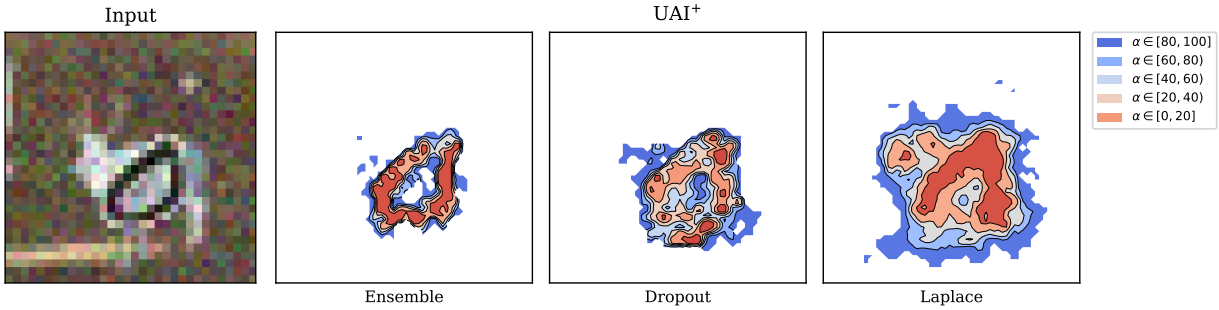

Figure 5: Illustration of UAI$^+$ method explanations based on Absolute Gradient explanation method for three different Bayesian scenarios: Deep Ensemble, MC Dropout and Laplace approximation. From the explanations we can observe the main features that each of the Bayesian Network used.

where I is the set containing all features and $O \subset I$ is a subset of features that are part of the segmented object itself.

While the AUC metric can be used both for explanation methods attributing positive and negative values, as well as for methods attributing just positive relevances, MA can only be used for positive relevances from the explanation method.

We acknowledge alternative metrics like Fidelity (Samek et al., 2016), ROAR (Hooker et al., 2019), and F-Fidelity (Zheng et al., 2024), which assess explanation quality via input perturbation. However, these are designed for deterministic models with a single explanation per prediction. Our method produces a distribution over explanations, making direct application of such metrics non-trivial. We therefore use object-localization metrics (AUC-ROC and MA), which are more naturally suited to our probabilistic setting. Extending fidelity-based metrics to BNNs remains an important direction for future work.

5.3 Baseline

In our experiments, we compare the proposed UAI explanations with the baseline explanation, which uses the expected value of the weights $\mathbb{E}[W]$. In practice, this would corresponds to a MAP classifier, e.g., Laplace approximation or MC Dropout, where the mean weights of the model are used for prediction. Hence, we refer to the baseline explanation as the one explaining the standard deterministic model using the mean weights — this allows us to draw conclusions regarding how standard explanation methods can be enhanced by "Bayesianisation".

6 Experiments

In the following, we demonstrate the performance of our proposed method both qualitatively and quantitatively.

6.1 Experiment on Custom MNIST data

We evaluate our proposed methods on the Custom MNIST (CMNIST) dataset (Bykov et al., 2021), where MNIST digits are plotted on a randomly chosen CIFAR background. This ensures that the decision-making basis for the model should rely only on the number and not on the randomly chosen background. Hence, using the available segmentations of the MNIST digits as a ground-truth indicator of the relevant area the evidence should be distributed to, we are able to measure the goodness of the different explanations. To show that our method is applicable to different types of Bayesian Neural Networks and Network Ensembles we analyze three different settings all based on the same standard Lenet architecture (LeCun et al., 1998). We employ three different Bayesian approximation methods — Deep Ensemble of 100 different networks,

trained with a random initialization respectively, Laplace approximation, and MC Dropout (more details about the model architecture and training parameters can be found in the appendix). Figure 5 illustrates the differences of UAI$^+$ explanations between the three Bayesian scenarios. For each of the three described scenarios, we used a test set of 10000 generated images, which was not used during training. For each image, $N = 100$ relevances were sampled using the LRP-ε method from the posterior distribution (in the case of a deep ensemble, each relevance came from a different network instance).

The quantitative results of the localization evaluation for all three scenarios are summarized in Table 2. From the results, we can observe that the Union method is best-performing in terms of AUC metric, while

Table 1: Quantitative results for Localisation (AUC) and Relevance Mass Accuracy (MA). Values are mean ± s.d. rounded to two decimals.

	Ensemble		**Laplace Approx.**		**Dropout**	
	AUC	MA	AUC	MA	AUC	MA
Random	0.50 ± 0.02	0.25 ± 0.01	0.50 ± 0.02	0.25 ± 0.01	0.50 ± 0.02	0.25 ± 0.01
Baseline	—	—	0.54 ± 0.03	0.85 ± 0.10	0.53 ± 0.03	0.92 ± 0.07
Average	0.50 ± 0.05	0.94 ± 0.05	0.50 ± 0.06	$\mathbf{0.85 \pm 0.09}$	0.51 ± 0.04	0.91 ± 0.07
Intersection ($\alpha = 5$)	0.16 ± 0.06	$\mathbf{1.00 \pm 0.00}$	0.15 ± 0.07	0.78 ± 0.41	0.17 ± 0.06	$\mathbf{0.99 \pm 0.03}$
Union ($\alpha = 95$)	$\mathbf{0.88 \pm 0.05}$	0.77 ± 0.09	$\mathbf{0.86 \pm 0.07}$	0.70 ± 0.13	$\mathbf{0.86 \pm 0.05}$	0.87 ± 0.08
UAI$^+$	0.79 ± 0.06	0.90 ± 0.08	0.78 ± 0.06	0.79 ± 0.14	0.71 ± 0.05	0.94 ± 0.07

the Intersection method shows overwhelmingly best results in terms of the Relevance Mass Accuracy metric. From these results we conclude that the Union method indeed is better in visualizing all the information the Bayesian Network has learned about the object, however, comparatively low MA scores of the Union method imply that explanations attribute positive relevance outside of the object of interest. In comparison, the Intersection method has low AUC scores in almost all scenarios, which implies that the Intersection method does not "cover" the object in interest with positive attributions, but high MA scores show high confidence in positive features — if the Intersection method attributes a positive relevance to a feature, it is most likely to lie inside of object of interest.

6.2 Experiment on ImageNet

We demonstrate the usefulness of the proposed method for explaining the decision-making process for a naturally non-Bayesian model that was trained with dropout regularization. We used the broadly applied pre-trained VGG16 network (Simonyan & Zisserman, 2014). This network was pre-trained on ImageNet (Russakovsky et al., 2015) and is naturally non-Bayesian. To access the uncertainty of this naturally non-Bayesian model, we employed MC Dropout (Gal & Ghahramani, 2016) during the test phase, which can be always applied when a model's architecture comprises at least one dropout layer. Furthermore, as relevance attribution function, we used the LRP-CMP rule as explainability method. For the evaluation of the performance of the proposed methods, we randomly choose a small subset of classes from the ImageNet dataset, consisting of 5 classes: "castle", "lemon", "llama", "wine" and "tiger cat". For each class we downloaded[2] 1000 random images. The explanation results for the Intersection, Average, Union, and UAI$^+$ explanation for three randomly chosen images are shown in Figure 6.

6.3 Experiment on real-world cancer data

In the following, we perform a binary classification experiment, where the task is to classify histopathological images into cancer and non-cancer images. Clearly, the domain of diagnostic pathology requires not only accurate and robust predictions, but most importantly, explanations and insights about why an image was classified as cancerous or not by the learning machine (cf. also Klauschen et al. (2018); Hägele et al. (2020); Binder et al. (2021)).

[2]To download a subset of ImageNet dataset, the following library was used: `https://github.com/mf1024/ImageNet-Datasets-Downloader`.

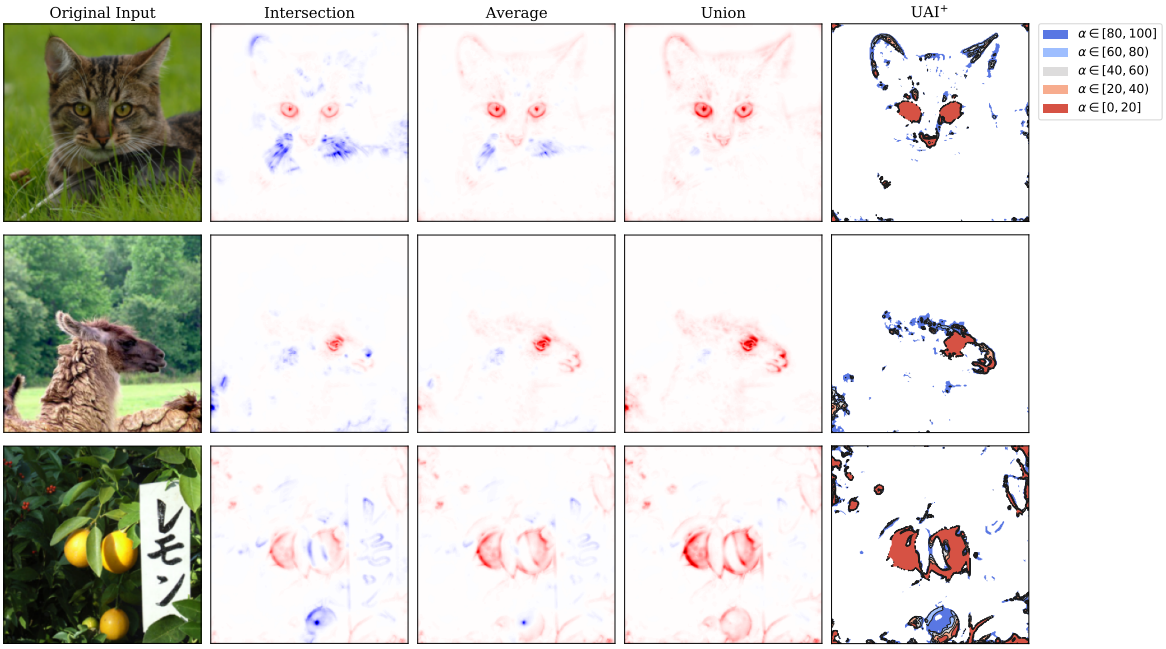

Figure 6: Exemplary explanations of three images taken from ImageNet (red/blue indicates positive/negative relevance). Each row corresponds to a particular input image. From left to right: original image, intersection explanation, baseline (average LRP) explanation, and Union explanations, as well as the UAI$^+$ explanation. We observe that the baseline explanation attributes positive relevance to almost the whole cat except the whiskers. The intersection explanation highlights solely the eyes and the nose of the cat as coherent features whereas the union explanation highlights the same features as the baseline explanation but additionally attributes relevance to the whiskers. The explanation of UAI$^+$ provides a holistic representation of the different feature importance regarding the model decision: red=high importance, (orange, grey, light blue)=intermediate importance, and dark blue=low importance.

The histopathological dataset consists of the 22302 patches of anonymized non-small-cell lung cancer (NSCLC) cases (n=200) from routine diagnostics from the archives of the Institute of Pathology at the Charité University Hospital which had been digitized using a 3DHistech P1000 whole slide scanner. The data had been annotated by board-certified pathologists for 28 different morphological classes ranging. For this experiment, we are interested only in the problem of binary classification for one class — carcinoma. The dataset is divided into 2 parts: training and testing. The training dataset consists of 17884 labeled patches, where 69.9% of the images are labeled as non-cancerous.

For this experiment, we trained a VGG-16 (Simonyan & Zisserman, 2014) network with an additional dropout regularization layer applied in the feature extractor part of the network (after the first and third MaxPool layer). The network was trained in a binary classification fashion for detecting the existence of cancer tissue in a histological slide. We trained the network for 100 epochs, using the cross-entropy loss with stochastic gradient descent, where the initial learning rate was set to 0.001. The trained network achieved an accuracy of 86.96% on the provided test dataset and an F1 score of 0.8205. Afterward, we computed the UAI explanations for different test images, which allows us to provide an additional estimate of the

Table 2: Localization results of different Bayesian explanations methods for detecting malignant cancer cells. We observe that the Union explanation with $\alpha = 99$ achieves the best performance in this experiment.

Method		AUC Score
Baseline		0.6534 ± 0.1705
Average		0.6635 ± 0.1712
UAI	$\alpha = 1$	0.5960 ± 0.1733
	$\alpha = 5$	0.6138 ± 0.1742
	$\alpha = 25$	0.6536 ± 0.1716
	$\alpha = 50$	0.6818 ± 0.1711
	$\alpha = 75$	0.7026 ± 0.1717
	$\alpha = 95$	0.7179 ± 0.1694
	$\alpha = 99$	**0.7201 ± 0.1680**

explanation uncertainty. Results for three different prototypical cancer images are shown in Figure 7. The original histopathological image is shown in the left column with the black dots representing expert-labeled cancerous cells.

In the right column of Figure 7, the UAI results are plotted over the original image and highlight the relevant parts of the image regarding their importance for the classifier. In the Intersection explanation (second column from the left) we show the regions, in the image where the classifier is most certain about their relevance to the prediction "cancer", and with gray color, features that are absent from the Average explanation are highlighted. Analogous, for Union explanation we highlight features in green, that are attributed positively in the Union explanation, but not in the Average explanation. Thus we can visually observe differences between Intersection, Average, and Union explanations — while Intersection explanations provide a user with more "conservative" explanations, the Union method allows us to observe all the features, that were considered with positive evidence towards the class in question. From the quantitative results shown in Table 2 we can observe that the higher the percentile value the larger the AUC score for the localization criteria of the cancerous cells. Note that in the quantitative experiment, we used only the images labeled as cancerous, where the annotations of the cancerous areas were available.

In general, the UAI-based heatmaps with different α values can prove particularly useful with respect to different diagnostic applications. Low α value explanations can help to identify tissue regions with the highest likelihood of cancer. High α percentile explanations may then be used for AI-based screening applications, where it is important not to overlook even the tiniest occurrence of tumor cells in tissue samples. Therefore, combining UAI analyses with low and high α may provide high sensitivity and simultaneously points the pathologists to regions where the machine is most confident about its decision. This additional information will improve diagnostic speed and also reduce the risk of overlooking crucial information in the diagnostic process.

6.4 Confirming the Clever Hans Effect

In this experiment, we revisit the work of Lapuschkin et al. (2019); Samek et al. (2021a) on the *Clever Hans* effect. This term refers to a problematic solution strategy in which a model achieves correct predictions for the wrong reasons. The name originates from a horse named Hans, which appeared to solve arithmetic problems, but was in fact responding to subtle cues from its trainer rather than performing actual calculations.

In modern machine learning, a *Clever Hans* effect typically involves the model relying on spurious correlations or artifacts—such as watermarks—that are coincidentally associated with specific classes. For instance, an irrelevant visual pattern might consistently appear in training images of one class, leading the model to learn this pattern as a discriminative feature (Lapuschkin et al., 2016; 2019).

We conducted our experiments on two datasets: Pascal VOC 2007 and ImageNet. Prior work (Lapuschkin et al., 2019) has shown that models trained on Pascal VOC 2007 exhibit Clever Hans behavior for the class *horse*, often relying on photographer watermarks. In the case of ImageNet, Bykov et al. (2023d) identified spurious correlations between Chinese-language watermarks and certain classes such as “carton” and “monitor”. For both experiments, we used the VGG16 architecture: a model retrained from scratch for Pascal VOC 2007 (see Appendix A.3.3) and a standard pretrained model for ImageNet.

Figure 8 presents the UAI explanations for both datasets. In both cases, watermarks appear prominently in the explanations within the top 5th percentile. This means that for at least 95% of the model samples, the model consistently identifies the watermark as a highly relevant feature for the respective class predictions. Specifically, Chinese watermarks are associated with “carton” and “monitor” in ImageNet, while photographer watermarks are linked to the “horse” class in Pascal VOC 2007.

These findings confirm the presence of the Clever Hans effect: the models rely on artifacts rather than semantically meaningful features. Importantly, our UAI method proves effective in identifying such systematic misbehaviors, helping to differentiate between robust explanations and potential artifacts of the explainability technique itself (see also (Dombrowski et al., 2019; Heo et al., 2019; Samek et al., 2019)).

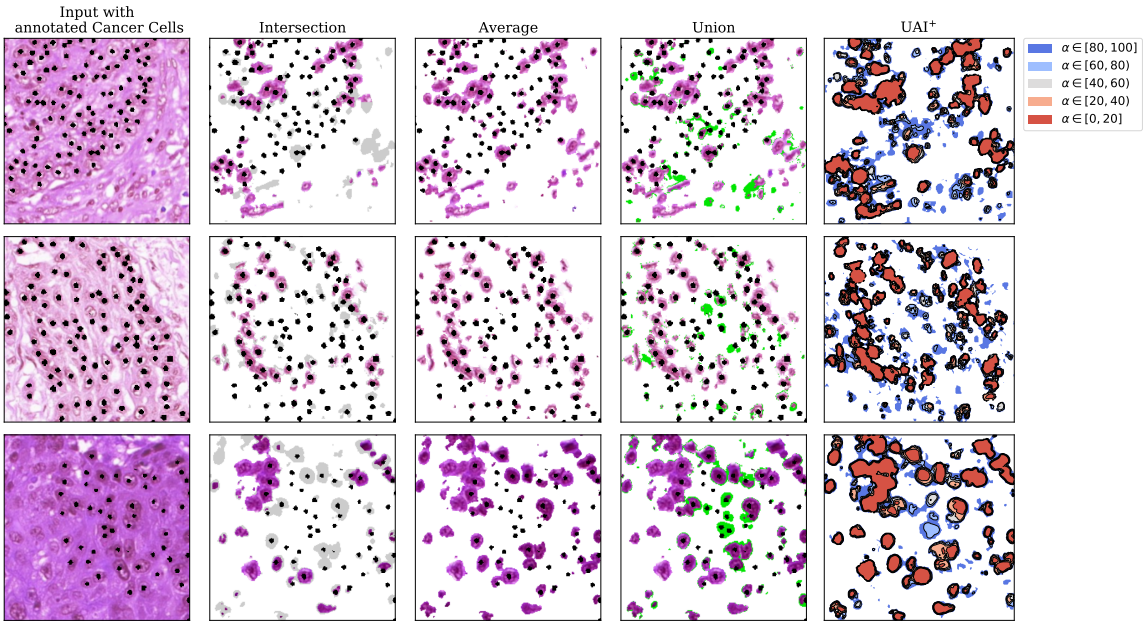

Figure 7: Comparison of the explanation results for the cancer experiment. A VGG16 (Simonyan & Zisserman, 2014) was trained on a set of Haematoxylin-eosin-stained Lung adeno carcinoma (LUAD) as well as on non cancer histological slides. Three original images labeled as cancer, taken from the test set, are shown on the left, overlaid with black dots, which represent the cancer cells annotated by experts. Behind, the various explanations of the model prediction for the class cancer are shown from left to right as intersection, baseline, union, and UAI$^+$ explanation. For reporting only significant positive relevances, we set a threshold at $\varepsilon = 0.05$ and visualize only relevances that surpass this threshold. We highlight by grey and green the additional information gained by our union and intersection approach in comparison to the baseline explanation. In detail, the intersection highlights the most certain areas, which are indicated as parts of the original image, whereas the areas that are not certain, and thus not visualized in the intersection explanation are highlighted in grey. In contrast, the union explanation identifies additional information, that was not shown in the baseline explanation and therefore may point out new areas that may be cancerous, which are highlighted in green. The aggregation of the diverse levels of feature importance is summarized in the UAI$_+$ explanation shown on the right.

7 Concluding Discussion

When tackling real-world learning problems, Bayesian models have been helpful in assessing the intrinsic uncertainties encountered when predicting. The field of XAI could introduce a further safety layer into the inference process when using neural networks because explanations can contribute to, e.g., unmasking flaws in a model or data set (Lapuschkin et al., 2019). So far, however, no XAI method for Bayesian Neural Networks was conceived.

In this paper, we have therefore connected the BNN model class (and their inbuilt uncertainty quantification) with XAI by proposing the (to the best of our knowledge) first practical method for explaining BNNs. As demonstrated, our novel technique (called UAI) is applicable to several popular explanation methods.

By appropriately averaging sampled relevance maps, we can obtain an explanation for the expected predictive function. This allows us to shed light on the decision-making process of BNNs: interestingly, UAI allows us to not only inspect the most relevant pixels for a decision but also their (un)certainties. Our method is thus a formidable starting point for obtaining novel insight into the behavior of Bayesian learning models.

We found that, with a high parameter range of α, UAI explains the behavior of the network more informatively, in comparison to a standard mean explanation baseline. By gauging α, users can understand the

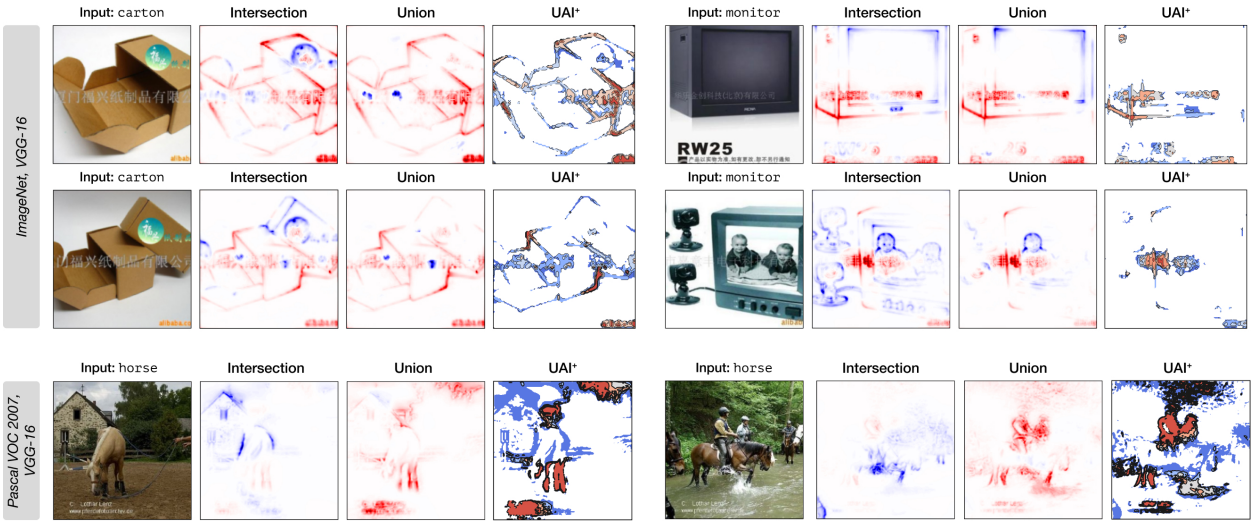

Figure 8: Illustrative visualization of the *Clever Hans* effect in two datasets: ImageNet and Pascal VOC 2007. The UAI explanations assist in distinguishing between random artifacts in the attribution maps and systematic behavior learned by the model. The enhanced method, UAI$^+$, allows us to confirm the Clever Hans effect with high confidence (highlighted in red) in both cases: for ImageNet, where a spurious correlation arises due to a Chinese-language watermark at the center of the image, and for Pascal VOC 2007, where the model relies on photographer watermarks containing name and website (bottom, left part of the images).

rationale behind a network: with small parameters of α, we can observe what features are considered to be contributing towards the prediction regardless of the sampled strategy (intersection explanation). With high parameters α, we can understand the features for which at least a small fraction of strategies attribute them with positive relevance (union explanation). Thus, by choosing the parameter α, users can choose between more or less risk-averse explanations, depending on the task objective. The proposed UAI explanation additionally helps to understand and reflect the multiple explanation modes inherent in a Bayesian ensemble (cf. Figure 2).

The computational complexity of our presented method is linear in the number of posterior samples. In practice, we found that as few as 100 samples are sufficient to obtain a stable assessment of explanation uncertainty, which keeps the computational cost low. While more samples can be used for finer-grained analysis, the default choice of 100 samples strikes a balance between accuracy and efficiency, which makes our approach feasible even for large-scale applications.

Limitations include: (i) conclusions are conditioned on the chosen posterior approximation (e.g., MC Dropout, Laplace) and do not claim recovery of true posterior multi-modality; (ii) fidelity-style metrics are not yet standardized for distributions of explanations; and (iii) a full human-in-the-loop evaluation is beyond our scope. We see adapting fidelity metrics to probabilistic explanations and controlled user studies as promising future work.

Concluding, our UAI framework now enables a wide range of explanation methods to analyze the complex, multi-faceted decision-making process of Bayesian Neural Networks. Moreover, this novel possibility of quantifying uncertainties in explanations of trained Neural Networks may become a profound help to mitigate risks in safety-critical applications. Future studies will focus further on clinical decision-making systems.

References

Amina Adadi and Mohammed Berrada. Peeking inside the black-box: a survey on explainable artificial intelligence (xai). *IEEE access*, 6:52138–52160, 2018.

Christopher J Anders, Grégoire Montavon, Wojciech Samek, and Klaus-Robert Müller. Understanding patch-based learning of video data by explaining predictions. In *Explainable AI: Interpreting, Explaining*

and Visualizing Deep Learning, pp. 297–309. Springer, 2019.

Leila Arras, Franziska Horn, Grégoire Montavon, Klaus-Robert Müller, and Wojciech Samek. " what is relevant in a text document?": An interpretable machine learning approach. *PloS one*, 12(8):e0181142, 2017.

Leila Arras, Ahmed Osman, and Wojciech Samek. Ground truth evaluation of neural network explanations with clevr-xai. *arXiv preprint arXiv:2003.07258*, 2020.

Sebastian Bach, Alexander Binder, Grégoire on, Frederick Klauschen, Klaus-Robert Müller, and Wojciech Samek. On pixel-wise explanations for non-linear classifier decisions by layer-wise relevance propagation. *PloS one*, 10(7), 2015.

David Baehrens, Timon Schroeter, Stefan Harmeling, Motoaki Kawanabe, Katja Hansen, and Klaus-Robert Müller. How to explain individual classification decisions. *Journal of Machine Learning Research*, 11(Jun): 1803–1831, 2010.

David Bau, Bolei Zhou, Aditya Khosla, Aude Oliva, and Antonio Torralba. Network dissection: Quantifying interpretability of deep visual representations. In *Proceedings of the IEEE conference on computer vision and pattern recognition*, pp. 6541–6549, 2017.

Alexander Binder, Michael Bockmayr, Miriam Hägele, Stephan Wienert, Daniel Heim, Katharina Hellweg, Masaru Ishii, Albrecht Stenzinger, Andreas Hocke, Carsten Denkert, et al. Morphological and molecular breast cancer profiling through explainable machine learning. *Nature Machine Intelligence*, 3(4):355–366, 2021.

Christopher M Bishop. *Pattern recognition and machine learning*. Springer, 2006.

Sébastien Bubeck, Varun Chandrasekaran, Ronen Eldan, Johannes Gehrke, Eric Horvitz, Ece Kamar, Peter Lee, Yin Tat Lee, Yuanzhi Li, Scott Lundberg, et al. Sparks of artificial general intelligence: Early experiments with gpt-4. *arXiv preprint arXiv:2303.12712*, 2023.

Varun H Buch, Irfan Ahmed, and Mahiben Maruthappu. Artificial intelligence in medicine: current trends and future possibilities. *British Journal of General Practice*, 68(668):143–144, 2018.

Vanessa Buhrmester, David Münch, and Michael Arens. Analysis of explainers of black box deep neural networks for computer vision: A survey. *arXiv preprint arXiv:1911.12116*, 2019.

Kirill Bykov, Anna Hedström, Shinichi Nakajima, and Marina M-C Höhne. Noisegrad: enhancing explanations by introducing stochasticity to model weights. *arXiv preprint arXiv:2106.10185*, 2021.

Kirill Bykov, Mayukh Deb, Dennis Grinwald, Klaus Robert Muller, and Marina MC Höhne. DORA: Exploring outlier representations in deep neural networks. *Transactions on Machine Learning Research*, 2023a. ISSN 2835-8856. URL `https://openreview.net/forum?id=nfYwRIezvg`.

Kirill Bykov, Laura Kopf, and Marina M-C Höhne. Finding spurious correlations with function-semantic contrast analysis. In *World Conference on Explainable Artificial Intelligence*, pp. 549–572. Springer, 2023b.

Kirill Bykov, Laura Kopf, Shinichi Nakajima, Marius Kloft, and Marina M-C Höhne. Labeling neural representations with inverse recognition. *arXiv preprint arXiv:2311.13594*, 2023c.

Kirill Bykov, Klaus-Robert Müller, and Marina M-C Höhne. Mark my words: Dangers of watermarked images in imagenet. *arXiv preprint arXiv:2303.05498*, 2023d.

Lucy R Chai. Uncertainty estimation in bayesian neural networks and links to interpretability. *Master of Philosophy (University of Cambridge)*, 2018.

Angel Cruz-Roa, Ajay Basavanhally, Fabio González, Hannah Gilmore, Michael Feldman, Shridar Ganesan, Natalie Shih, John Tomaszewski, and Anant Madabhushi. Automatic detection of invasive ductal carcinoma in whole slide images with convolutional neural networks. In *Medical Imaging 2014: Digital Pathology*, volume 9041, pp. 904103. International Society for Optics and Photonics, 2014.

Arun Das and Paul Rad. Opportunities and challenges in explainable artificial intelligence (xai): A survey. *arXiv preprint arXiv:2006.11371*, 2020.

PS De Laplace. Mémoire sur les suites récurro-récurrentes et sur leurs usages dans la théorie des hasards. *Mém. Acad. Roy. Sci. Paris*, 6:353–371, 1774.

Jia Deng, Wei Dong, Richard Socher, Li-Jia Li, Kai Li, and Li Fei-Fei. Imagenet: A large-scale hierarchical image database. In *2009 IEEE conference on computer vision and pattern recognition*, pp. 248–255. Ieee, 2009.

Ann-Kathrin Dombrowski, Maximillian Alber, Christopher Anders, Marcel Ackermann, Klaus-Robert Müller, and Pan Kessel. Explanations can be manipulated and geometry is to blame. In *Advances in Neural Information Processing Systems*, pp. 13567–13578, 2019.

Ann-Kathrin Dombrowski, Christopher J Anders, Klaus-Robert Müller, and Pan Kessel. Towards robust explanations for deep neural networks. *Pattern Recognition*, pp. 108194, 2021.

Dumitru Erhan, Yoshua Bengio, Aaron Courville, and Pascal Vincent. Visualizing higher-layer features of a deep network. *University of Montreal*, 1341(3):1, 2009.

Tom Fawcett. An introduction to roc analysis. *Pattern Recogn. Lett.*, 27(8):861–874, June 2006. ISSN 0167-8655. doi: 10.1016/j.patrec.2005.10.010. URL `https://doi.org/10.1016/j.patrec.2005.10.010`.

Y. Gal and Z. Ghahramani. Dropout as a Bayesian approximation: Representing model uncertainty in deep learning. In *Proceedings of ICML*, 2016.

Robert Geirhos, Jörn-Henrik Jacobsen, Claudio Michaelis, Richard Zemel, Wieland Brendel, Matthias Bethge, and Felix A Wichmann. Shortcut learning in deep neural networks. *Nature Machine Intelligence*, 2(11):665–673, 2020.

Alex Graves. Practical variational inference for neural networks. In J. Shawe-Taylor, R. Zemel, P. Bartlett, F. Pereira, and K.Q. Weinberger (eds.), *Advances in Neural Information Processing Systems*, volume 24. Curran Associates, Inc., 2011. URL `https://proceedings.neurips.cc/paper_files/paper/2011/file/7eb3c8be3d411e8ebfab08eba5f49632-Paper.pdf`.

Dennis Grinwald, Kirill Bykov, Shinichi Nakajima, and Marina MC Höhne. Visualizing the diversity of representations learned by bayesian neural networks. *Transactions on Machine Learning Research*, 2023.

Miriam Hägele, Philipp Seegerer, Sebastian Lapuschkin, Michael Bockmayr, Wojciech Samek, Frederick Klauschen, Klaus-Robert Müller, and Alexander Binder. Resolving challenges in deep learning-based analyses of histopathological images using explanation methods. *Scientific reports*, 10:6423, 2020.

Kaiming He, Xiangyu Zhang, Shaoqing Ren, and Jian Sun. Delving deep into rectifiers: Surpassing human-level performance on imagenet classification. In *Proceedings of the IEEE international conference on computer vision*, pp. 1026–1034, 2015.

Dan Hendrycks and Kevin Gimpel. A baseline for detecting misclassified and out-of-distribution examples in neural networks. *arXiv preprint arXiv:1610.02136*, 2016.

Juyeon Heo, Sunghwan Joo, and Taesup Moon. Fooling neural network interpretations via adversarial model manipulation. *Advances in Neural Information Processing Systems*, 32:2925–2936, 2019.

Andreas Holzinger, Georg Langs, Helmut Denk, Kurt Zatloukal, and Heimo Müller. Causability and explainability of artificial intelligence in medicine. *Wiley Interdisciplinary Reviews: Data Mining and Knowledge Discovery*, 9(4):e1312, 2019.

Sara Hooker, Dumitru Erhan, Pieter-Jan Kindermans, and Been Kim. A benchmark for interpretability methods in deep neural networks. *Advances in neural information processing systems*, 32, 2019.

Matthias Humt, Jongseok Lee, and Rudolph Triebel. Bayesian optimization meets laplace approximation for robotic introspection. *arXiv preprint arXiv:2010.16141*, 2020.

Pavel Izmailov, Polina Kirichenko, Nate Gruver, and Andrew G Wilson. On feature learning in the presence of spurious correlations. *Advances in Neural Information Processing Systems*, 35:38516–38532, 2022.

Andrew Janowczyk and Anant Madabhushi. Deep learning for digital pathology image analysis: A comprehensive tutorial with selected use cases. *Journal of pathology informatics*, 7, 2016.

Pieter-Jan Kindermans, Kristof T Schütt, Maximilian Alber, Klaus-Robert Müller, Dumitru Erhan, Been Kim, and Sven Dähne. Learning how to explain neural networks: Patternnet and patternattribution. *arXiv preprint arXiv:1705.05598*, 2017.

D. P. Kingma, T. Salimans, and M. Welling. Variational dropout and the local reparameterization trick. In *Advances in NIPS*, 2015.

Frederick Klauschen, K-R Müller, Alexander Binder, Michael Bockmayr, M Hägele, P Seegerer, Stephan Wienert, Giancarlo Pruneri, S de Maria, S Badve, et al. Scoring of tumor-infiltrating lymphocytes: From visual estimation to machine learning. In *Seminars in cancer biology*, volume 52, pp. 151–157. Elsevier, 2018.

Maximilian Kohlbrenner, Alexander Bauer, Shinichi Nakajima, Alexander Binder, Wojciech Samek, and Sebastian Lapuschkin. Towards best practice in explaining neural network decisions with lrp, 2020.

Jeamin Koo, Jungsuk Kwac, Wendy Ju, Martin Steinert, Larry Leifer, and Clifford Nass. Why did my car just do that? explaining semi-autonomous driving actions to improve driver understanding, trust, and performance. *International Journal on Interactive Design and Manufacturing (IJIDeM)*, 9(4):269–275, 2015.

Yongchan Kwon, Joong-Ho Won, Beom Joon Kim, and Myunghee Cho Paik. Uncertainty quantification using bayesian neural networks in classification: Application to biomedical image segmentation. *Computational Statistics & Data Analysis*, 142:106816, 2020.

Sebastian Lapuschkin, Alexander Binder, Grégoire Montavon, Klaus-Robert Müller, and Wojciech Samek. Analyzing classifiers: Fisher vectors and deep neural networks. In *Proceedings of the IEEE Conference on Computer Vision and Pattern Recognition*, pp. 2912–2920, 2016.

Sebastian Lapuschkin, Stephan Wäldchen, Alexander Binder, Grégoire on, Wojciech Samek, and Klaus-Robert Müller. Unmasking clever hans predictors and assessing what machines really learn. *Nature communications*, 10:1096, 2019.

Yann LeCun, Léon Bottou, Yoshua Bengio, and Patrick Haffner. Gradient-based learning applied to document recognition. *Proceedings of the IEEE*, 86(11):2278–2324, 1998.

Jongseok Lee, Matthias Humt, Jianxiang Feng, and Rudolph Triebel. Estimating model uncertainty of neural networks in sparse information form. In *International Conference on Machine Learning (ICML)*. Proceedings of Machine Learning Research, 2020.

B Léon. Online algorithms and stochastic approximations. *Online Learning and Neural Networks; Cambridge University Press: Cambridge, UK*, 1998.

Zhiheng Li, Ivan Evtimov, Albert Gordo, Caner Hazirbas, Tal Hassner, Cristian Canton Ferrer, Chenliang Xu, and Mark Ibrahim. A whac-a-mole dilemma: Shortcuts come in multiples where mitigating one amplifies others. In *Proceedings of the IEEE/CVF Conference on Computer Vision and Pattern Recognition*, pp. 20071–20082, 2023.

Xiaodong Liu, Pengcheng He, Weizhu Chen, and Jianfeng Gao. Improving multi-task deep neural networks via knowledge distillation for natural language understanding. *arXiv preprint arXiv:1904.09482*, 2019.

Scott M Lundberg and Su-In Lee. A unified approach to interpreting model predictions. In *Advances in neural information processing systems*, pp. 4765–4774, 2017.

Scott M. Lundberg, Gabriel Erion, Hugh Chen, Alex DeGrave, Jordan M. Prutkin, Bala Nair, Ronit Katz, Jonathan Himmelfarb, Nisha Bansal, and Su-In Lee. From local explanations to global understanding with explainable ai for trees. *Nature Machine Intelligence*, 2(1):2522–5839, 2020.

Laurens van der Maaten and Geoffrey Hinton. Visualizing data using t-sne. *Journal of machine learning research*, 9(Nov):2579–2605, 2008.

W. J. Maddox, P. Izmailov, T. Garipov, D. P. Vetrov, and A. G. Wilson. A simple baseline for bayesian uncertainty in deep learning. In *Advances in NeurIPS*, 2019.

Amil Merchant, Simon Batzner, Samuel S Schoenholz, Muratahan Aykol, Gowoon Cheon, and Ekin Dogus Cubuk. Scaling deep learning for materials discovery. *Nature*, pp. 1–6, 2023.

D. Molchanov, A. Ashukha, and D. Vetrov. Variational dropout sparsifies deep neural networks. In *Proceedings of ICML*, 2017.

Grégoire Montavon, Wojciech Samek, and Klaus-Robert Müller. Methods for interpreting and understanding deep neural networks. *Digital Signal Processing*, 73:1–15, 2018.

Grégoire Montavon, Alexander Binder, Sebastian Lapuschkin, Wojciech Samek, and Klaus-Robert Müller. Layer-wise relevance propagation: an overview. In *Explainable AI: Interpreting, Explaining and Visualizing Deep Learning*, pp. 193–209. Springer, 2019.

Jesse Mu and Jacob Andreas. Compositional explanations of neurons. *Advances in Neural Information Processing Systems*, 33:17153–17163, 2020.

Anh Nguyen, Alexey Dosovitskiy, Jason Yosinski, Thomas Brox, and Jeff Clune. Synthesizing the preferred inputs for neurons in neural networks via deep generator networks. In *Advances in neural information processing systems*, pp. 3387–3395, 2016.

Tuomas Oikarinen and Tsui-Wei Weng. Clip-dissect: Automatic description of neuron representations in deep vision networks. *arXiv preprint arXiv:2204.10965*, 2022.

K. Osawa, S. Swaroop, A. Jain, R. Eschenhagen, R. E. Turner, R. Yokota, and M. E. Khan. Practical deep learning with Bayesian principles. In *Advances in NeurIPS*, 2019.

Hippolyt Ritter, Aleksandar Botev, and David Barber. A scalable laplace approximation for neural networks. In *6th International Conference on Learning Representations, ICLR 2018-Conference Track Proceedings*, volume 6. International Conference on Representation Learning, 2018.

Olga Russakovsky, Jia Deng, Hao Su, Jonathan Krause, Sanjeev Satheesh, Sean Ma, Zhiheng Huang, Andrej Karpathy, Aditya Khosla, Michael Bernstein, et al. Imagenet large scale visual recognition challenge. *International journal of computer vision*, 115(3):211–252, 2015.

Rabia Saleem, Bo Yuan, Fatih Kurugollu, Ashiq Anjum, and Lu Liu. Explaining deep neural networks: A survey on the global interpretation methods. *Neurocomputing*, 2022.

Wojciech Samek, Alexander Binder, Grégoire on, Sebastian Lapuschkin, and Klaus-Robert Müller. Evaluating the visualization of what a deep neural network has learned. *IEEE transactions on neural networks and learning systems*, 28(11):2660–2673, 2016.

Wojciech Samek, Grégoire Montavon, Andrea Vedaldi, Lars Kai Hansen, and Klaus-Robert Müller (eds.). *Explainable AI: Interpreting, Explaining and Visualizing Deep Learning*, volume 11700 of *Lecture Notes in Computer Science*. Springer, 2019.

Wojciech Samek, Grégoire Montavon, Sebastian Lapuschkin, Christopher J. Anders, and Klaus-Robert Müller. Explaining deep neural networks and beyond: A review of methods and applications. *Proceedings of the IEEE*, 109(3):247–278, 2021a.

Wojciech Samek, Grégoire Montavon, Sebastian Lapuschkin, Christopher J Anders, and Klaus-Robert Müller. Explaining deep neural networks and beyond: A review of methods and applications. *Proceedings of the IEEE*, 109(3):247–278, 2021b.

Ramprasaath R Selvaraju, Michael Cogswell, Abhishek Das, Ramakrishna Vedantam, Devi Parikh, and Dhruv Batra. Grad-cam: Visual explanations from deep networks via gradient-based localization. In *Proceedings of the IEEE international conference on computer vision*, pp. 618–626, 2017.

David Silver, Aja Huang, Chris J Maddison, Arthur Guez, Laurent Sifre, George Van Den Driessche, Julian Schrittwieser, Ioannis Antonoglou, Veda Panneershelvam, Marc Lanctot, et al. Mastering the game of go with deep neural networks and tree search. *nature*, 529(7587):484–489, 2016.

Karen Simonyan and Andrew Zisserman. Very deep convolutional networks for large-scale image recognition. *arXiv preprint arXiv:1409.1556*, 2014.

Karen Simonyan, Andrea Vedaldi, and Andrew Zisserman. Deep inside convolutional networks: Visualising image classification models and saliency maps. *arXiv preprint arXiv:1312.6034*, 2013.

Daniel Smilkov, Nikhil Thorat, Been Kim, Fernanda Viégas, and Martin Wattenberg. Smoothgrad: removing noise by adding noise. *arXiv preprint arXiv:1706.03825*, 2017.

Nitish Srivastava, Geoffrey Hinton, Alex Krizhevsky, Ilya Sutskever, and Ruslan Salakhutdinov. Dropout: a simple way to prevent neural networks from overfitting. *The journal of machine learning research*, 15(1): 1929–1958, 2014.

Mukund Sundararajan, Ankur Taly, and Qiqi Yan. Axiomatic attribution for deep networks. *arXiv preprint arXiv:1703.01365*, 2017.

Erico Tjoa and Cuntai Guan. A survey on explainable artificial intelligence (xai): Toward medical xai. *IEEE Transactions on Neural Networks and Learning Systems*, 2020.

Marina M-C Vidovic, Nico Görnitz, Klaus-Robert Müller, Gunnar Rätsch, and Marius Kloft. Opening the black box: Revealing interpretable sequence motifs in kernel-based learning algorithms. In *Joint European Conference on Machine Learning and Knowledge Discovery in Databases*, pp. 137–153. Springer, 2015.

Marina M-C Vidovic, Nico Görnitz, Klaus-Robert Müller, and Marius Kloft. Feature importance measure for non-linear learning algorithms. *arXiv preprint arXiv:1611.07567*, 2016.

Oriol Vinyals, Timo Ewalds, Sergey Bartunov, Petko Georgiev, Alexander Sasha Vezhnevets, Michelle Yeo, Alireza Makhzani, Heinrich Küttler, John Agapiou, Julian Schrittwieser, et al. Starcraft ii: A new challenge for reinforcement learning. *arXiv preprint arXiv:1708.04782*, 2017.

Ulrike Von Luxburg. A tutorial on spectral clustering. *Statistics and computing*, 17(4):395–416, 2007.

F. Wenzel, K. Roth, B. S. Veeling, J. Swiatkowski, L. Tran, S. Mandt, J. Snoek, T. Salimans, R. Jenatton, and S. Nowozin. How good is the bayes posterior in deep neural networks really? *arXiv:2002.02405*, 2020.

Gesa Wiegand, Matthias Schmidmaier, Thomas Weber, Yuanting Liu, and Heinrich Hussmann. I drive-you trust: Explaining driving behavior of autonomous cars. In *Extended Abstracts of the 2019 CHI Conference on Human Factors in Computing Systems*, pp. 1–6, 2019.

A. G. Wilson and P. Izmailov. Bayesian deep learning and a probabilistic perspective of generalization. In *Advances in NeurIPS*, 2020.

Andrew Gordon Wilson. The case for bayesian deep learning. *arXiv preprint arXiv:2001.10995*, 2020.

Dong-Ok Won, Klaus-Robert Müller, and Seong-Whan Lee. An adaptive deep reinforcement learning framework enables curling robots with human-like performance in real-world conditions. *Science Robotics*, 5 (46), 2020.

Han Xiao, Kashif Rasul, and Roland Vollgraf. Fashion-mnist: a novel image dataset for benchmarking machine learning algorithms. *arXiv preprint arXiv:1708.07747*, 2017.

Jason Yosinski, Jeff Clune, Anh Nguyen, Thomas Fuchs, and Hod Lipson. Understanding neural networks through deep visualization. *arXiv preprint arXiv:1506.06579*, 2015.

Jianming Zhang, Sarah Adel Bargal, Zhe Lin, Jonathan Brandt, Xiaohui Shen, and Stan Sclaroff. Top-down neural attention by excitation backprop. *International Journal of Computer Vision*, 126(10):1084–1102, 2018.

Xu Zheng, Farhad Shirani, Zhuomin Chen, Chaohao Lin, Wei Cheng, Wenbo Guo, and Dongsheng Luo. F-fidelity: A robust framework for faithfulness evaluation of explainable ai. *arXiv preprint arXiv:2410.02970*, 2024.

A Appendix

In the following, we provide the supplementary material to our paper Explaining Bayesian Neural Networks.

A.1 Proof of Theorem 1

Proof. For LRP-0, it holds that

$$R_W(x) = \mathcal{T}_x[f_W](x), \tag{10}$$

with $\mathcal{T}_x[f_W](x) = x \odot \nabla_x[f_W](x)$. Furthermore, the linearity

$$\tau_1 \mathcal{T}_x[f_1](x) + \tau_2 \mathcal{T}_x[f_2](x) = \mathcal{T}_x[\tau_1 f_1 + \tau_2 f_2](x)$$

holds for any $\tau_1, \tau_2 \in \mathbb{R}$ and any weakly differentiable functions f_1, f_2 except at the non-strongly-differentiable points of f_1 and f_2. We will prove, that in this case

$$\mathcal{T}_x \left[\mathbb{E}_W \left[f_W\right]\right](x) = \mathbb{E}_W \left[\mathcal{T}_x[f_W](x)\right] \tag{11}$$

holds except for measure zero points.

Let us fix x. If f_W is strongly differentiable at x for all W on the support of its posterior distribution $q(W)$, linearity of $\mathcal{T}_x$ holds and therefore Equation 11 holds due to Lemma 1. Let us define

$$\mathcal{W}_x = \{W; f_W \text{ is not strongly differentiable at } x\}, \quad \mathcal{Z} = \{x; \int \delta(W \in \mathcal{W}_x) q(W) dW > 0\},$$

where $\delta(\cdot)$ denotes the Dirac measure. Equation 11 still holds for $x \in \overline{\mathcal{Z}}$, because the contribution from the set of non-differentiable models at x is zero. For any bounded distribution $q(x)$ in the input space, it holds that

$$\int q(x) \int \delta(W \in \mathcal{W}_x) q(W) dW dx = \int q(W) \int q(x) \delta(W \in \mathcal{W}_x) dx dW = 0$$

due to the weakly differentiable assumption on f_W. This implies that $\mathcal{Z}$ is a measure zero set, which proves the claim for LRP-0.

Similarly, the gradient explanation, as well as IG, can be written as equation 10 with an operator $\mathcal{T}_x$ linear on all strongly-differentiable-points, and the same discussion applies to proving the claim. □

A.2 Details of the clustering procedure

For the image classification task we employ the SpRAy algorithm as follows (Lapuschkin et al., 2019):

1. **Relevance maps sampling**

   A collection $\{R_i\}_{i=1}^N$ of relevance maps is sampled from the posterior distribution.

2. **Preprocessing of the relevance maps.**

   All relevance maps are normalized using the MinMax normalization procedure. If needed, all relevance maps should be made uniform in shape and size, for future clustering.

   To speed up the clustering process and to produce more robust results we propose to use downsampling methods on the collection of samples. While the user is free to choose any dimensionality reduction method, we propose to use the Average Pooling method in order to achieve visually different strategies in different clusters.

3. **Spectral Cluster (SC) analysis on pre-processed relevance maps.**

   Pre-processed relevance maps are clustered by Spectral Clustering (SC) method. The affinity matrix, which is necessary for SC method, is based on k-nearest-neighborhood relationships. More detailed,

the affinity matrix $M = (m_{ij})_{i,j=1,...,N}$, measures the similarity $m_{ij} \geq 0$ between all N samples R_i and R_j of a source dataset and is constructed in the following way:

$$m_{ij} = \begin{cases} 1 & \text{if } R_i \text{ is among the k nearest neighbors of } R_j \\ 0 & \text{else} \end{cases}$$

Since this rule is asymmetric, the symmetric affinity matrix M is created by taking $m_{ij} = max(m_{ij}, m_{ji})$. Authors of the original paper highlight that similar clustering results were obtained using the Euclidean distance, with only small differences in the eigenvalue spectra.

The Laplacian L is computed from M as follows :

$$d_i = \sum_j m_{ij}.$$

$$D = diag\left[d_1, d_2, ..., d_N\right].$$

$$L = D - M.$$

The Matrix D is a diagonal matrix, which describe the measure of connectivity of a particular sample i with D being a diagonal matrix with entries d_{ii} describing the degree (of connectivity) of a sample i (Lapuschkin et al., 2019).

4. **Identification of interesting clusters by eigengap analysis**

   By performing an eigenvalue decomposition on the Laplacian L, eigenvalues $\lambda_1, \lambda_2, ..., \lambda_N$ are obtained. The number of eigenvalues $\lambda_i = 0$ identifies the number of (completely) disjoint clusters within the analyzed set of data.

   The final step of SpRAy assigns cluster labels to the data points, which can then be performed using an (arbitrary) clustering method: in our work we use k-means clustering on the N eigenvectors. The number of clusters can be obtained by *eigengap* analysis (Von Luxburg, 2007): it can be identified by eigenvalues close to zero as opposed to exactly zero, followed by an eigengap — rapid increase in the difference between two eigenvalues in the sequence $|\lambda_{i+1}\lambda_i|$ (Lapuschkin et al., 2019).

A.3 Experimental setup

A.3.1 CMNIST experiment

For the CMNIST experiment we used a simple convolutional network similar to LeNet (LeCun et al., 1998). For the Ensemble and for the Laplace scenarios a standard architecture was used, with only a change in number of input channels adjusted to 3-dimensional RGB inputs. For the Dropout scenario, after 2 Average Pooling layers, a 2-d Dropout layer was inserted with a dropout probability set to 0.25. 2 1D Dropout layers were added in the classification part of the network, with the probability of dropout set to 0.5.

All of the networks were trained with a batch size of 32, and with a Stochastic Gradient Descent algorithm, (Léon, 1998) with a learning rate of 0.01 and 0.9 momentum. A learning rate scheduler was used with the number of steps set to 7 and multiplicative parameter $\gamma = 0.1$. For the Ensemble scenario 100 networks were trained for 20 epochs, and for the Laplace and Dropout the number of epochs was set to 100. For the Laplace approximation, KFAC Laplace approximation was used (Humt et al., 2020; Lee et al., 2020), with Laplace regularization hyperparameters (additive and multiplicative) both set to 0.1.

A.3.2 Carcinoma experiment

For the Cancer experiment, we employed a standard VGG-16 (Simonyan et al., 2013) with additional 2D Dropout layers after each MaxPooling layer, with the probability of dropout set to 0.1 and 2 1D

Dropout layers in the classificator part of the network after each activation function with the probability of 0.5. The network was trained with SGD with 0.001 learning rate and 0.9 momentum. torch.optim.lr_scheduler.ReduceLROnPlateau learning rate scheduler was used with the factor of 0.1 and patience of 10.

A.3.3 Clever Hans experiment

For the Pascal VOC 2007 multi-label classification experiment, we employed a standard VGG16 network (Simonyan & Zisserman, 2014), and adjusted the number of output neurons from 1000 to 20, which is the number of different classes in the Pascal VOC 2007 dataset.

We resized each training image, such that the shorter axis has 224 pixels, keeping the aspect ratio unchanged. Then, we randomly cropped the longer axis and obtained square images with the size 224×224. We trained the network for 60 epochs, by minimizing the Binary Cross Entropy loss preceded with a Sigmoid layer[3]. We used the Adam optimizer with its parameters set to $\alpha = 0.0001, \beta_1 = 0.9, \beta_2 = 0.999$. Our trained VGG16 network achieves 91.6%[4] in the multi-label classification on the test set, for which center cropping with square size of 224×224 was applied, instead of random cropping.

A.3.4 Fashion MNIST experiment

For the Fashion MNIST experiment we trained a LeNet network with 2 2D Dropout layers with $p = 0.5$ added after each of the Average Polling layers in the feature extractor part of the Network, and 1 1D Dropout layer with $p = 0.5$ after the Flatten Layer. The network was trained on FashionMNIST dataset with several augmentations, such as Color Jittering, Random Affine Transformations, and Random Horizontal Flips. The batch size was set to 64, the Network was trained using the Cross-Entropy loss for 50 epochs with Adam optimizer with standard parameters and a learning rate of 0.001.

[3] https://pytorch.org/docs/master/generated/torch.nn.BCEWithLogitsLoss.html
[4] https://scikit-learn.org/stable/modules/generated/sklearn.metrics.accuracy_score.html